INTERNATIONAL JOURNAL FOR NUMERICAL METHODS IN ENGINEERING
Int. J. Numer. Meth. Engng 2016; **108**:156–180

A Cartesian parametrization for the numerical analysis of material instability

A. Mota[1], Q. Chen[2,*,†], J.W. Foulk III[1], J.T. Ostien[1] and Z. Lai[2]

[1] *Mechanics of Materials Department, Sandia National Laboratories, Livermore, CA 94550, USA*
[2] *Glenn Department of Civil Engineering, Clemson University, Clemson, SC 29634, USA*

SUMMARY

We examine four parametrizations of the unit sphere in the context of material stability analysis by means of the singularity of the acoustic tensor. We then propose a Cartesian parametrization for vectors that lie a cube of side length two and use these vectors in lieu of unit normals to test for the loss of the ellipticity condition. This parametrization is then used to construct a tensor akin to the acoustic tensor. It is shown that both of these tensors become singular at the same time and in the same planes in the presence of a material instability. The performance of the Cartesian parametrization is compared against the other parametrizations, with the results of these comparisons showing that in general, the Cartesian parametrization is more robust and more numerically efficient than the others. Copyright © 2016 John Wiley & Sons, Ltd.

Received 29 October 2015; Revised 26 January 2016; Accepted 26 January 2016

KEY WORDS: material stability; constitutive equations; Newton methods; variational methods

1. INTRODUCTION

The numerical analysis of material instability plays an important role in the understanding and simulation of material failure in solid mechanics problems. A reliable and efficient method to determine the onset of material instability and the bifurcation directions is required whether one is interested in studying the instability itself or in devising numerical methods to regularize the solution at the onset of the instability [1–7].

Herein, we adopt the classical definition of material instability as the loss of the *strong ellipticity condition*. This is equivalent to the loss of the *strong Legendre–Hadamard condition* for stored energy densities that are twice continuously differentiable [8]. Loss of ellipticity has also been associated with the discontinuous acceleration of propagating waves by [9]. We use the term *acoustic* tensor for the second-order tensor associated with the strong ellipticity condition, which is also known as the *localization* tensor. Although this latter denomination may be more accurate, throughout this work, we use the former for historical reasons.

The determination of the loss of the strong ellipticity condition for a very general class of materials can be achieved by recourse to incremental variational constitutive updates. Within this framework, an incremental stress potential embodies the constitutive behavior of the material during a time increment, including elasticity, viscoelasticity, viscoplasticity, and rate dependence [10–16]. By using incremental variational constitutive updates, the stress and the tangent moduli can be derived from a hyperleastic-like potential for constitutive behavior that may include viscosity and rate dependence. This in turn provides the means to apply the tools developed herein for complex inelastic materials.

---

*Correspondence to: Qiushi Chen, Glenn Department of Civil Engineering, Clemson University, Clemson, SC 29634, USA.

†E-mail: qiushi@clemson.edu

1.1. Previous work

Extensive work has been carried out on the subject of material instabilities. The basic theoretical principles follow from the seminal work of [17] on elastic stability and were later extended to the inelastic regime by [18], [9], and others. The work of [19] and [20], among others, tied the instability in the constitutive description of homogeneous deformation to the onset of localized deformation, which was linked to the loss of the positive definiteness of the acoustic tensor of the material at a given state. See also Armero [4] and Garikipati and Miehe *et al.* [12] for a brief historical overview of the development of classical localization analysis.

In the context of finite element analysis, existing approaches to detect material instability as well as the bifurcation directions generally fall into two categories: analytical and numerical.

For certain material models under specific loading conditions, analytical solutions of the instability problem can be derived. For instance, Schreyer and Neilsen [21] derived an analytical criterion for the loss of ellipticity for a general class of symmetric constitutive equations. Becker [22] used the Gurson constitutive model in combination with a failure criterion based on material stability and bifurcation in a finite element model to predict fracture and fragmentation in a dynamic expanding ring experiment. Oliver and Huespe [23] provided closed-form solutions for the detection of the singularity of the acoustic tensor for a wide class of small deformation isotropic and anisotropic damage models. On the basis of the general Hadamard instability criterion, Xue and Belytschko [24] derived a closed-form expression to determine the onset of instability and the bifurcation directions for a particular damage plasticity model. These analytical approaches are computationally very efficient and robust and avoid the pitfall of the inability to find global minima [25].

Closed-form solutions, however, are not available for more complicated material models under general loading conditions, which motivates the development and implementation of numerical approaches. Among the works that address the numerical resolution of material instability are those of Ortiz and coworkers [26, 27]. Ortiz *et al.* [27] formulated the detection of instability as a constrained minimization problem. A two-step procedure is proposed, wherein a sampling is performed over the parametric space of possible bifurcation directions followed by an iterative solution scheme using a Lagrange multiplier to enforce the unit-vector constraint. The algorithm was applied to the bifurcation analysis of a small deformation isotropic elastoplastic material model. Khen *et al.* [28] formulated the localization criterion for finite deformation plasticity in a Lagrangian formulation and searched the bifurcation direction using two characteristic angles in a spherical coordinate system. Boussaa and Aravas [29] proposed an alternative approach where numerical and symbolic computations were combined to detect the loss of strong ellipticity and applied this approach to a Gurson-type porous material. Mosler [30] proposed a numerical algorithm based on sampling the discrete parametric space and using the minimum of the sampling as initial guess for a Newton method to find a better approximation to the exact minimum of the determinant of the acoustic tensor and corresponding bifurcation directions. More recently, Oliver *et al.* [25] developed a new efficient algorithm based on the iterative solution of a coupled eigenvalue problem in terms of the acoustic tensor. The algorithm is very efficient and accurate for symmetric cases, where the material tangent has both major and minor symmetries. For cases that lack minor symmetries, however, the algorithm only gives an approximation, which limits its applicability to finite deformation material models, or non-associative plasticity material models.

Compared with analytical approaches, numerical algorithms are more general in the sense that they can be applied to different material models under different loading conditions, for both two-dimensional and three-dimensional problems. The drawbacks are also clear; however, they are much more computationally demanding and less robust. The convergence of an iterative method is sensitive to the initial guess, for instance. In the context of a nonlinear finite element analysis, the material instability condition has to be tested at every integration point and at every time step, and therefore, both the computational efficiency and robustness of any numerical algorithm used for its detection become a major concern.

In this work, we use a sampling-based algorithm followed by a Newton iterative method to solve the minimization problem associated with the strong ellipticity condition for the detection of material instability. We present several parametrizations for the representation of the unit normal vector used to construct the acoustic tensor. The hypothesis is that the parametrization of this normal vector significantly affects the computation time and robustness of the numerical solution algorithm. To this end, we propose a new Cartesian parametrization to construct a tensor akin to the acoustic tensor and compare its performance and robustness against other four parametrizations. The numerical algorithms developed in this work are general and can be applied to both small and finite deformation material models with symmetric or non-symmetric tangents. To that end, we analyze idealized isotropic and anisotropic damage models subjected to simplified loadings. The resulting landscapes for minimization are sufficiently rich and differentiating to provide meaningful quantified evaluations of the proposed parametrizations.

2. GENERAL FRAMEWORK

Incremental variational constitutive updates provide the means to determine the loss of the strong ellipticity condition for a very general class of materials. Within this framework, the constitutive behavior of the material during a time increment is characterized by an incremental stress potential that may include elasticity, viscoelasticity, viscoplasticity, and rate dependence [10–16]. See Appendix A.

Within this framework, the stress and the tangent moduli can be derived from the hyperleastic-like potential (A.11) for a very general class of constitutive behavior that may include viscosity and rate dependence. This in turn provides the means to apply the classical analysis tools that are used in hyperelasticity, such as the strong ellipticity condition, for complex inelastic materials as well.

2.1. *The strong ellipticity condition*

The ellipticity condition can be expressed as follows:

$$(\boldsymbol{m} \otimes \boldsymbol{n}) : \mathbb{A} : (\boldsymbol{m} \otimes \boldsymbol{n}) \geqslant 0, \quad \forall\, \boldsymbol{m}, \boldsymbol{n} \in \mathbb{R}^3 \tag{1}$$

where the tangent moduli $\mathbb{A}$ are defined in (A.13). Note that for simplicity in notation and unless otherwise stated, henceforth, we omit the time indices n and $n+1$ with the understating that further developments take place at time t_{n+1}. If condition (1) holds strictly for nonzero vectors $\boldsymbol{m}$ and $\boldsymbol{n}$, then it is called the strong ellipticity condition [12, 17, 31]. It is customary to *assume* that $\boldsymbol{m}$ and $\boldsymbol{n}$ are unit vectors, that is, $\boldsymbol{m}, \boldsymbol{n} \in S^2$ where $S^2 := \{t \in \mathbb{R}^3 \mid \|\boldsymbol{t}\| = 1\}$ is the unit sphere. Define

$$\begin{aligned} \boldsymbol{n} \cdot \mathbb{A} &:= \boldsymbol{n}_p A_{pjkl} e_j \otimes e_k \otimes e_l, & \boldsymbol{n} \circ \mathbb{A} &:= \boldsymbol{n}_p A_{ipkl} e_i \otimes e_k \otimes e_l, \\ \mathbb{A} \circ \boldsymbol{n} &:= \boldsymbol{n}_p A_{ijpl} e_i \otimes e_j \otimes e_l, & \mathbb{A} \cdot \boldsymbol{n} &:= \boldsymbol{n}_p A_{ijkp} e_i \otimes e_j \otimes e_k, \end{aligned} \tag{2}$$

and the acoustic tensor as follows:

$$\boldsymbol{A} := \boldsymbol{n} \circ \mathbb{A} \cdot \boldsymbol{n} \quad \text{or} \quad A_{ik}\, e_i \otimes e_k := n_j A_{ijkl} n_l\, e_i \otimes e_k, \quad \boldsymbol{n} \in S^2, \tag{3}$$

then the strong ellipticity condition becomes

$$\boldsymbol{m} \cdot \boldsymbol{A} \cdot \boldsymbol{m} > 0, \quad \boldsymbol{m} \in S^2. \tag{4}$$

In order to satisfy the strong ellipticity condition, the acoustic tensor must be positive definite. Therefore, (1) and (4) reduce to

$$\det \boldsymbol{A} > 0, \tag{5}$$

which provides a method to determine the onset of a material instability.

2.2. *Bifurcation*

By using the strong ellipticity condition (1) or its equivalent with the acoustic tensor (5), the detection of bifurcation or loss of ellipticity in the material is fully characterized by its fourth-order tangent moduli (A.13). The onset of bifurcation is then posed as a minimization problem. First, we assume that the normal vector $\boldsymbol{n}$ is parametrized by a set of parameters q, thus turning the determinant of the acoustic tensor $\det A$ into a function of q. Then the determinant of the acoustic tensor $\det A(q)$ is minimized with respect to q. Thus, the loss of strong ellipticity may be stated as follows:

$$f(q) := \det \boldsymbol{A}(q), \quad \min_{q} f(q) = 0, \quad \boldsymbol{n}(q) \in S^2. \tag{6}$$

If the determinant function $f(q)$ is differentiable, the minimization problem can be rewritten equivalently as follows:

$$\frac{\partial f}{\partial q}(q) = 0, \tag{7}$$

which can be solved by standard numerical optimization techniques, for example, a Newton-type iterative procedure.

3. PARAMETRIZATIONS FOR BIFURCATION ANALYSIS

Efficient computation of the minimization problem (7) requires a careful choice of the parametrization for the normal vector $\boldsymbol{n}(q) \in S^2$, which is equivalent to selecting a parametrization for the unit sphere. This choice has a significant effect on the complexity of the determinant function $f(q)$ and its derivatives with respect to q needed to solve the optimization problem. Herein, five different options are explored. The first four (spherical, stereographic, projective, and tangent) are indeed parametrizations of the unit sphere. The last parametrization, which we term Cartesian, relaxes the restriction that the normal vector be an element of the unit sphere. We describe the parametrizations in detail next, assuming that a Cartesian frame of reference originates from the center of each one.

3.1. Spherical parametrization

This parametrization is the most commonly used in numerical bifurcation analysis, for example, [30, 32–34]. In the spherical parametrization, elements $\boldsymbol{n}$ of the unit sphere S^2 are simply parametrized by their spherical coordinates with polar angle $\varphi \in [0, \pi]$, azimuthal angle $\theta \in [0, \pi]$, and radial distance $r = \|\boldsymbol{n}\| = 1$. The reduced range in the angle θ is due to symmetry of the bifurcation condition, as for this purpose $\boldsymbol{n}$ and $-\boldsymbol{n}$ yield the same result; see Figure 1a. In terms of the canonical basis,

$$\boldsymbol{n}(\varphi, \theta) := \left\{ \begin{array}{c} \sin\varphi\cos\theta \\ \sin\varphi\sin\theta \; . \\ \cos\varphi \end{array} \right\}. \tag{8}$$

3.2. Stereographic parametrization

The unit sphere is parametrized with the aid of an equatorial plane as shown in Figure 1b. Consider a point P that is both on this plane and on a line that passes through the north pole Q of the sphere and the tip of the vector $\boldsymbol{n}$. The Cartesian coordinates x and y of P provide the desired parametrization, which can be easily derived by finding the intersection of the line and the sphere. The upper hemisphere can be ignored because of the symmetry of the bifurcation condition, thus avoiding the singularity in parametrizing a normal vector that points to the north pole Q. The normal vector n in terms of the canonical basis is as follows:

$$\boldsymbol{n}(x, y) := \left\{ \begin{array}{c} \frac{2x}{x^2+y^2+1} \\ \\ \frac{2y}{x^2+y^2+1} \; . \\ \\ \frac{x^2+y^2-1}{x^2+y^2+1} \end{array} \right\} \tag{9}$$

where the parameters $x \in [-1, 1]$ and $y \in [-1, 1]$.

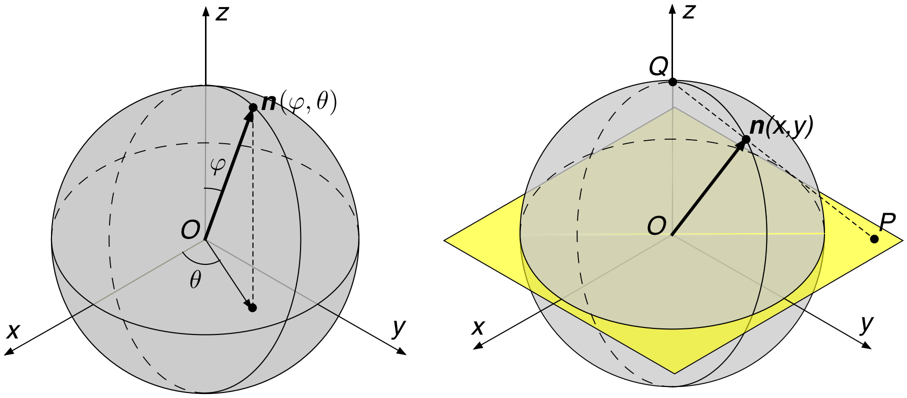

(a) Spherical **(b)** Stereographic

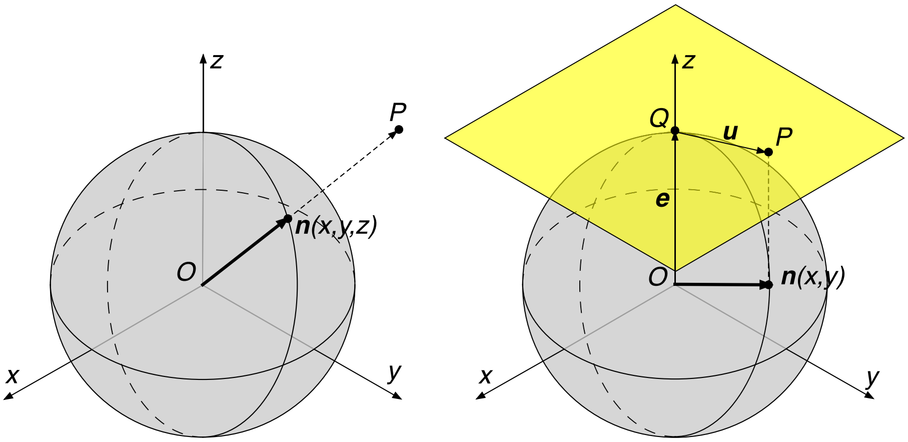

(c) Projective **(d)** Tangent

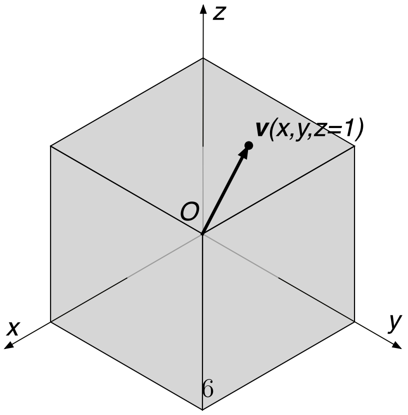

(e) Cartesian

Figure 1. The five parametrizations used for the detection of loss of ellipticity.

3.3. *Projective parametrization*

In the projective parametrization, the norm of the position vector of a point P with respect to the center of the sphere is constrained to obtain a unit vector $\boldsymbol{n}$ [27]. This is equivalent to projecting the point P onto the unit sphere S^2, as shown in Figure 1. The normalization is affected by means of a constraint enforced by a Lagrange multiplier as follows:

DOI: 10.1002/nme

$$\boldsymbol{n}(x, y, z) := \begin{Bmatrix} x \\ y \\ z \end{Bmatrix} \text{ subjected to } x^2 + y^2 + z^2 = 1 \tag{10}$$

where the parameters $x \in [-1, 1]$, $y \in [-1, 1]$ and $z \in [-1, 1]$.

3.4. Tangent parametrization

This parametrization of the unit sphere is defined by a tangent plane [35]. Let $u \in \mathbb{R}^3$ be the position vector of the point P in the tangent plane with respect to the contact point Q between the sphere and the plane; then let $e \in S^2$ be the position vector of the contact point Q with respect to the center of the sphere O, as shown in Figure 1d. Define a rotation vector $\vec{\theta} := e \times u$; then the rotation angle is $\theta := \left\| \vec{\theta} \right\| \equiv \|u\|$. Let also $\check{\vec{\theta}} \in so(3)$ be the skew-symmetric tensor such that $\check{\vec{\theta}} \cdot v \equiv \vec{\theta} \times v \ \forall \ v \in \mathbb{R}^3$. The expression for the exponential map for $\check{\vec{\theta}}$ is as follows:

$$\exp \check{\vec{\theta}} := \begin{Bmatrix} I \in SO(3), & \text{if } \theta = 0; \\ I + \frac{\sin\theta}{\theta}\check{\vec{\theta}} + \frac{(1-\cos\theta)}{\theta^2}\check{\vec{\theta}}^2 \in SO(3), & \text{if } \theta > 0; \end{Bmatrix}, \tag{11}$$

which is often accredited to Rodrigues [36]. Next, define

$$\exp_e u := \exp \check{\vec{\theta}} \cdot e = \cos\theta e + \frac{\sin\theta}{\theta} u \in S^2. \tag{12}$$

The parametrization follows immediately by setting the contact point Q to the north pole of the sphere, that is, $e = [0, 0, 1]^T$ and $u = [x, y, 0]^T$ with the normal vector n given by the following:

$$\boldsymbol{n} = \exp_e u \in S^2, \tag{13}$$

which leads to a more explicit representation for the normal vector in the canonical basis as follows:

$$\boldsymbol{n}(x, y) := \begin{Bmatrix} \dfrac{x \sin\sqrt{x^2 + y^2}}{\sqrt{x^2 + y^2}} \\ \dfrac{y \sin\sqrt{x^2 + y^2}}{\sqrt{x^2 + y^2}} \\ \cos\sqrt{x^2 + y^2} \end{Bmatrix}. \tag{14}$$

where the parameters $x \in [-\pi/2, \pi/2]$ and $y \in [-\pi/2, \pi/2]$. Note that although the normal vector n is a unit vector, the position vector on the tangent plane $u = [x, y, 0]^T$ is not subjected to the constraint $x^2 + y^2 + z^2 = 1$ and the range $[-\pi/2, \pi/2]$ is sufficient for the position vector to cover all points on the plane.

3.5. Cartesian parametrization

The previous four are parametrizations of the unit sphere. Here, we propose a new parametrization, termed Cartesian, where the restriction that the normal vector be of unit length is relaxed. To set the stage for the Cartesian parametrization, we revisit the strong ellipticity condition

$$(u \otimes v) : \mathbb{A} : (u \otimes v) > 0, \quad \forall\, u, v \in \mathbb{R}^3 \setminus \{0\}. \tag{15}$$

Note that this condition only requires that the vectors u and v be nonzero. Thus, the condition that they belong to the unit sphere S^2 may be relaxed. In analogy to the classical acoustic tensor (3), define

$$B := v \circ \mathbb{A} \cdot v \quad \text{or} \quad B_{ik}\, e_i \otimes e_k := v_j\, A_{ijkl}\, v_l\, e_i \otimes e_k, \quad v \in \mathbb{R}^3 \setminus \{0\}; \tag{16}$$

thus, the strong ellipticity condition may be expressed as follows:

$$u \cdot B \cdot u > 0, \quad u \in \mathbb{R}^3 \setminus \{0\}. \tag{17}$$

As in (5), the strong ellipticity condition becomes

$$\det B > 0. \tag{18}$$

Proposition 1
The tensor B from (16) leads to the same bifurcation condition as the acoustic tensor A from (3), that is, if the minimum for $\det A$ is equal to zero for a vector $a \in S^2$, then the minimum for $\det B$ is also zero for a vector $b \in \mathbb{R}^3 \setminus \{0\}$ that is parallel to a.

Proof
Introduce the bijective map $g : \mathbb{R}^3 \setminus \{0\} \mapsto S^2 \times \mathbb{R}^+$ that allows the representation of nonzero vectors in $\mathbb{R}^3$ as unit vectors in the unit sphere (direction) and the corresponding nonzero norm (magnitude). Then define

$$v \in \mathbb{R}^3 \setminus \{0\}, \quad v := \|v\| \in \mathbb{R}^+, \quad \boldsymbol{n} := \frac{v}{v} \in S^2; \tag{19}$$

therefore, from (4) and (17),

$$B(v, \boldsymbol{n}) = v^2 A(\boldsymbol{n}) \quad \text{and} \quad \det B(v, \boldsymbol{n}) = v^6 \det A(\boldsymbol{n}). \tag{20}$$

Now, let the bifurcation condition for A be

$$\min_{n} \det A(\boldsymbol{n}) = 0, \quad a := \arg\min_{n} \det A(\boldsymbol{n}) \in S^2 \implies \det A(n) > 0\, \forall\, \boldsymbol{n} \neq a; \tag{21}$$

then it follows from (20) that

$$\det B(s, a) = 0, \quad \det B(s, \boldsymbol{n}) > 0, \quad \forall\, \boldsymbol{n} \neq a \text{ and } \forall\, s \in \mathbb{R}^+, \tag{22}$$

which means that

$$\min_{v,n} \det B(v, \boldsymbol{n}) = 0, \quad \{s, a\} := \arg\min_{v,n} \det B(v, \boldsymbol{n})\, \forall\, s \in \mathbb{R}^+, \tag{23}$$

as required. □

In order to remove the multiple minima associated with the arbitrary value of the scalar parameter s and obtain a parametrization, we restrict the range of the Cartesian coordinates such that $||v||_\infty$=1 and set the normal vector to

$$v(x, y, z) := \begin{cases} [x, y, 1]^T, & \text{if} x \in [-1, 1] \text{ and } y \in [-1, 1)]; \\ [1, y, z]^T, & \text{if } y \in [-1, 1] \text{ and } z \in [-1, 1); \\ [x, 1, z]^T, & \text{if } z \in [-1, 1] \text{ and } x \in [-1, 1); \\ [1, 1, 1]^T, & \text{otherwise.} \end{cases} \tag{24}$$

This confines the normal vector to the cube of side length two centered at the origin as shown in Figure 1e. Only three faces of the cube need to be considered because of the symmetry of the bifurcation condition.

The spherical parametrization commonly used in bifurcation analysis has a singularity at the poles as the azimuthal angle θ can adopt any value at those points. This leads to numerical diffculties when minima lie near or at the poles. The Cartesian parametrization advocated here does not contain any singularities of this kind.

4. BIFURCATION DETECTION

Within an incremental update setting, the numerical detection of the bifurcation condition for each time increment using any of the parametrizations just described consists of the following two steps:

- An initial sampling is performed over the parametric space for q for the normal vector $\boldsymbol{n} \in S^2$ or $v \in \left\{u \in \mathbb{R}^3 | \, ||u||_\infty = 1\right\}$ associated with the parametrization. This leads to a rough estimate of the minimum of the determinant function (6) and the associated bifurcation directions.
- The coarse estimate can be used to initiate an iterative procedure to find a more accurate estimate of the onset of bifurcation and its associated directions by solving the optimization problem (7).

In an actual finite element simulation, the previous two-step procedure may not yield estimates of the bifurcation condition that are accurate enough within a time increment, in particular if the size of the increment is relatively large. One way to improve the solution is to introduce adaptive time increments for the detection of the bifurcation condition. Define

$$\mu_{n+1,k} := \min_q f_{n+1,k}(q) = \min_q \det B_{n+1,k}(q) \tag{25}$$

where the tensor $B_{n+1,k}(q)$ may be either the one from (3) or the one from (16), depending on the parametrization in use and the index $n+1, k$ indicates that the evaluation occurs at time $t_{n+1,k} \in [t_n, t_{n+1}]$ for a kth adaptive iteration.

Consider the original time increment from t_n to t_{n+1}, where $\mu_n > 0$ and $\mu_{n+1} < 0$. This means that between time t_n and t_{n+1}, the strong ellipticity condition is violated and, hence, the material exhibits bifurcation. Assume also that $\mu_n/\mu_0 > \epsilon$, where μ_0 is the value of the determinant function evaluated at time t_0 and ϵ is a target tolerance. We wish to find a better estimate for the determinant function $\mu_{n+1,k}$, and hence the bifurcation time $t_{n+1,k}$, such that $\mu_{n+1,k}/\mu_0 \leqslant \epsilon$. This is achieved by an adaptive time increment procedure by means of bisection, as shown in Algorithm 1. This algorithm repeatedly decreases the time increment in half until the convergence criterion $\mu_{n+1,k}/\mu_0 \leqslant \epsilon$ is met.

Algorithm 1 AdaptiveStep($\mu_0, \mu_{n+1}, t_{n+1}, \epsilon$)

```
Require: $\mu_{n+1} < 0$
Ensure: $\mu_{n+1,k} \in [0, \epsilon\mu_0]$
  initialize $k \leftarrow 1, \quad \alpha \leftarrow \frac{1}{2}, \quad \triangle t \leftarrow t_{n+1} - t_n, \quad \mu_{n+1,k} \leftarrow \mu_{n+1}$
  while $\mu_{n+1,k} < 0$ or $\mu_{n+1,k}/\mu_0 > \epsilon$ do
    $t_{n+1,k} \leftarrow t_n + \alpha \triangle t$
    compute $F(t_{n+1,k})$ using the global solution scheme
    compute $\triangle Z(t_{n+1,k})$ by solving (A.12)
    compute $\mathbb{A}(t_{n+1,k})$ using (A.13)
    compute $\mu_{n+1,k}$ by solving (25)
    if $\mu_{n+1,k} > 0$ then
      $\alpha \leftarrow \alpha + 2^{-k-1}$
    else
      $\alpha \leftarrow \alpha - 2^{-k-1}$
    end if
    $k \leftarrow k + 1$
  end while
```

The adaptive time increment procedure allows the accurate (up to the tolerance ϵ) detection of the bifurcation time during a loading process. The procedure described in this section to detect material bifurcation can be applied to a very general class of materials, and its numerical performance is demonstrated in the following section.

5. NUMERICAL EXAMPLES

The performance and applicability of the proposed Cartesian and the other four parametrizations are examined by using them for the bifurcation analysis of two material models under different loading conditions. The analysis is performed at the material point level. Of particular interest are the robustness and computational efficiency of the different parametrizations.

5.1. *Small deformation isotropic elastic damage model*

We start the bifurcation analysis on a simple small deformation isotropic damage model. The model formulation is briefly presented first. The material model is then subjected to simple shear to determine the performance of the different parametrizations on the detection of material bifurcation.

5.1.1. Model formulation. The stress and constitutive tangent of the small deformation isotropic damage model are derived from the strain-energy function that has the form

$$A(\epsilon, \xi) := \frac{1}{2}(1-\xi)\epsilon : \mathbb{C}^{\mathrm{e}} : \epsilon \tag{26}$$

where ϵ is the infinitesimal strain tensor, $\mathbb{C}^{\mathrm{e}}$ is the fourth-order elastic moduli tensor, and ξ is a damage parameter introduced to trigger material bifurcation. For isotropic linear elasticity, the elastic moduli tensor $\mathbb{C}^{\mathrm{e}}$ is given as follows:

$$\mathbb{C}^{\mathrm{e}} := \lambda I \otimes I + 2\mu\mathbb{I} \tag{27}$$

where λ and μ are the Lamé constants, I is the second-order identity tensor, and $(\mathbb{I})_{ijkl} = \frac{1}{2}(\delta_{ik}\delta_{jl} + \delta_{il}\delta_{jk})$ is the fourth-order symmetric identity tensor with δ_{ik} being the Kronecker delta.

We adopt the following evolution law for the scalar damage parameter ξ [37]

$$\xi(\alpha) := \xi_\infty[1 - \exp(-\alpha/\tau)] \tag{28}$$

where ξ_∞ describes the dimensionless maximum damage and τ is referred to as the damage saturation parameter. The parameter α is the maximum thermodynamic force [37] with the same dimensions as the effective strain energy. Within the closed time interval $[0, t]$, α is given as follows:

$$\alpha(t) := \max_{s\in[0,t]} A_0(s) \tag{29}$$

where $A_0(s)$ is the undamaged strain energy at time s.

Given the strain-energy function (26) and the damage evolution (28), the fourth-order tangent moduli tensor can be obtained by differentiating the strain-energy function with respect to the strain measure ϵ^{e} twice, which results in

$$\mathbb{C} := (1-\xi)\mathbb{C}^{\mathrm{e}} - \beta\frac{\partial\xi}{\partial\alpha}(\sigma_0 \otimes \sigma_0) \tag{30}$$

where σ_0 is the effective (undamaged) Cauchy stress and $\beta = 1 \Leftrightarrow \dot{\alpha} > 0$, $\beta = 0$ otherwise. In a small deformation setting, this tangent can be used to compute the acoustic tensor (3), which can then be tested for material bifurcation.

DOI: 10.1002/nme

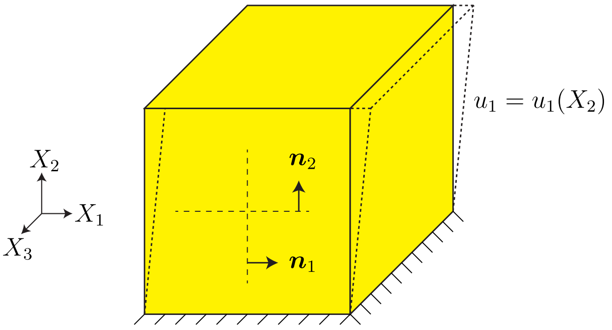

Figure 2. Schematic of the the applied loading for simple shear for infinitesimal deformations. The solution bifurcates on planes with normals n_1 and n_2.

5.1.2. Simple shear test. In this section, a simple shear test illustrated in Figure 2 is simulated with the following material properties: $\lambda = 80$, $\mu = 80$, $\xi_\infty = 1.0$, and $\tau = 1.0$. The resulting shear stress and shear strain are plotted in Figure 3a. The softening response is due to the evolution of the introduced damage parameter ξ. For the numerical detection of material bifurcation, the two-step procedure described in Section 4 is adopted, that is, (1) an initial sampling performed over the parametric space and (2) a Newton iterative procedure to obtain a better estimate of the onset of bifurcation and its associated directions. Figure 3b shows the degradation of the determinant $\det A$ for all five parametrizations up to the point when material bifurcation is detected. When $\det A = 0$, the material model bifurcates. In this example, all five parametrizations detect bifurcation at the same time, that is, when the shear strain $\epsilon_{12} = 0.0559$ as marked in Figure 3a. With the adaptive time-step algorithm, the precise time of bifurcation, up to the specified tolerance, can be detected.

While all five parametrizations detect bifurcation at the same time, Figure 3b provides little information on their computational efficiency and robustness, which are the focus of this work. The computation time of bifurcation detection mainly consists of two parts: (1) the computation time of the initial sampling over the parametric space and (2) the computation time of the Newton iterative scheme.

The computation time of the initial sampling depends on the number of sampling points or, equivalently, the density of the initial sampling grid. The denser the initial sampling grid, the more expensive it is computationally to perform a complete pass of all the points in the grid. The computation time for the Newton iterative scheme, on the other hand, depends mainly on the complexity of the objective function, that is, $\det A$, as well as the quality of the initial guess.

To compare the computation times of different parametrizations, we record the time spent on the bifurcation detection at a particular loading increment, for example, at the increment leading to bifurcation. We also vary the density of the initial sampling grid to determine its effect on different parametrizations. The density of the initial sampling grid is represented by the sampling interval and the number of sampling points, as shown in Figure 4.

A robust parametrization should be insensitive to the initial sampling grid. The computation time results are summarized in Table I. The table only shows the number of sampling points, N, along one dimension of the parametric space. Assuming the same number of intervals for each parameter, the total number of sampling points is N^D where D is the total dimension of the parametric space.

As expected, it can be seen from Table I that as the number of sampling points N per dimension decreases, so does the computation time. The spherical and the Cartesian parametrizations are the most efficient. The stereographic, projective, and tangent parametrizations are more computationally expensive. In the extreme case with $N = 1$, that is, only one initial sampling point, the stereographic, projective, and tangent parametrizations fail to correctly detect bifurcation, shown as a dash in the table.

As mentioned before, the choice of parametrization directly affects the complexity of the objective function $\det A$ in (7). This in turn affects the computational efficiency and robustness of the different parametrizations for the detection of material bifurcation, as shown in Table I. To illustrate this point, the landscapes of the objective function $\det A$ at bifurcation, that is, at $\epsilon_{12} = 0.0559$ are shown in

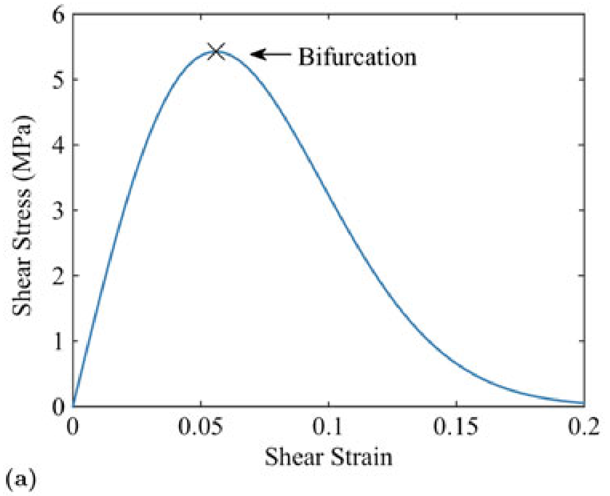

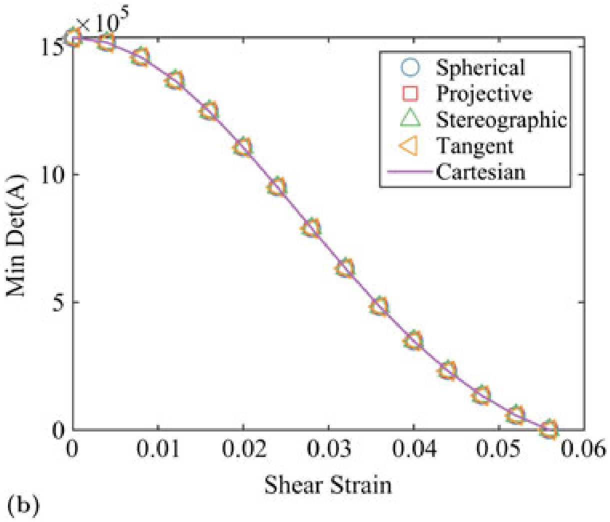

Figure 3. Simple shear test on small deformation isotropic damage model: (a) stress strain behavior, with the X indicating bifurcation, and (b) degradation of det A for different parametrizations upto the point material bifurcates ($\epsilon_{12} = 0.0559$).

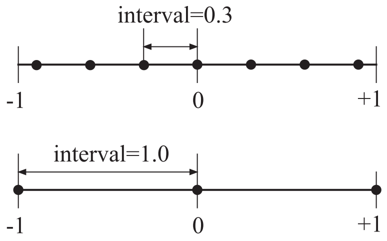

Figure 4. Schematic drawing shows the interval along one dimension of the normalized parameter space $[-1, 1]$ for the cases of interval = 0.3 (top) and interval = 1.0 (bottom). Black solid circles indicate the locations of grid points

Figure 5. The corresponding plane views of the determinant landscapes are shown in Figure 6, where the white stars indicate global minima. The projective parametrization requires three parameters, and therefore, it is not shown.

It is clear from these landscape plots that the complexity of the shape of the determinant function depends greatly on the choice of parametrization. Even for the very simple small deformation

DOI: 10.1002/nme

Table I. Computation time of the different parametrizations for the simple shear test in the loading increment leading to bifurcation.

Sampling		Run time (μs)				
Interval	Points	Spherical	Stereographic	Projective	Tangent	Cartesian
0.05	41	318	155	5636	226	347
0.1	21	124	89	884	107	115
0.2	11	70	60	183	64	81
0.3	7	63	184	178	157	39
0.4	5	73	181	197	145	27
0.5	5	51	37	88	53	27
0.6	3	62	174	200	215	23
0.7	3	61	180	188	188	23
0.8	3	50	170	188	144	24
0.9	3	51	177	156	159	23
1.0	3	47	37	79	51	23
1.5	1	51	–	–	–	21

The dash '–' indicates that the parametrization fails to detect bifurcation in this loading increment.

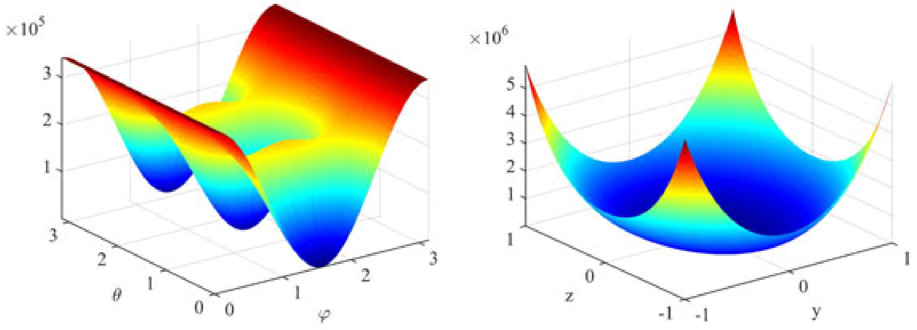

(a) Spherical (b) Cartesian

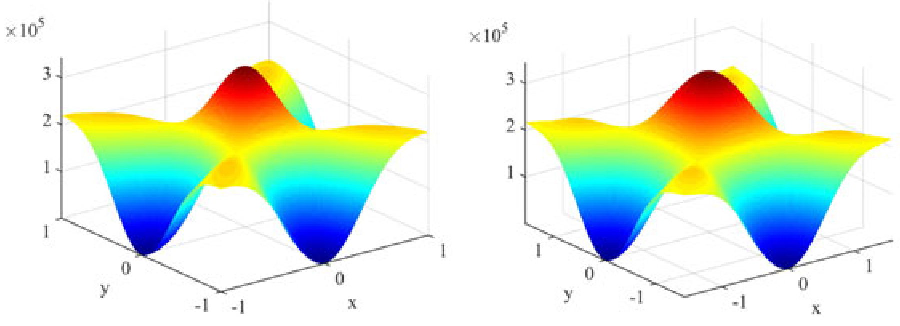

(c) Stereographic (d) Tangent

Figure 5. Landscapes of the determinant of the acoustic tensor at bifurcation for simple shear for the small deformation isotropic damage model. The normals to the planes of bifurcation are $n_1 = (1, 0, 0)$ and $n_2 = (0, 1, 0)$.

isotropic model adopted in this example, the landscape of the determinant function can be quite complex as in the cases of the spherical, stereographic, and tangent parametrizations.

The Cartesian parametrization results in a simple bowl-shaped objective function, which renders the Newton iterative scheme to be particularly robust and insensitive to the initial guess. Evidence for this can be seen in Table I as the Cartesian and spherical parametrizations are the only ones able to detect bifurcation when the sampling grid is reduced to a single point.

We now elaborate further on the robustness of the parametrizations by considering the situation in which the initial sampling is eliminated altogether. In the absence of the initial sampling, a random

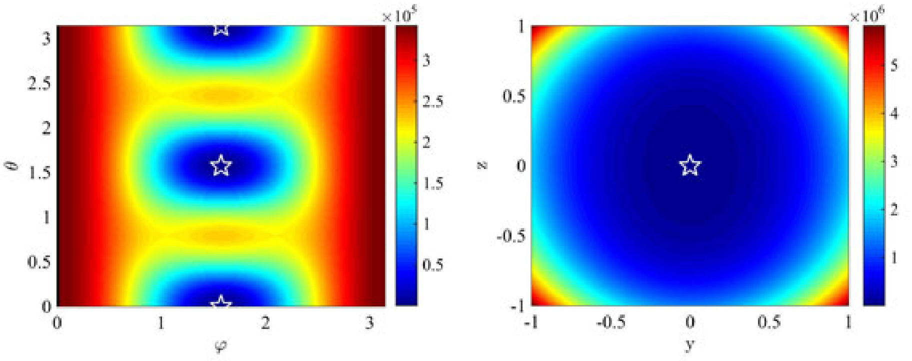

(a) Spherical (b) Cartesian

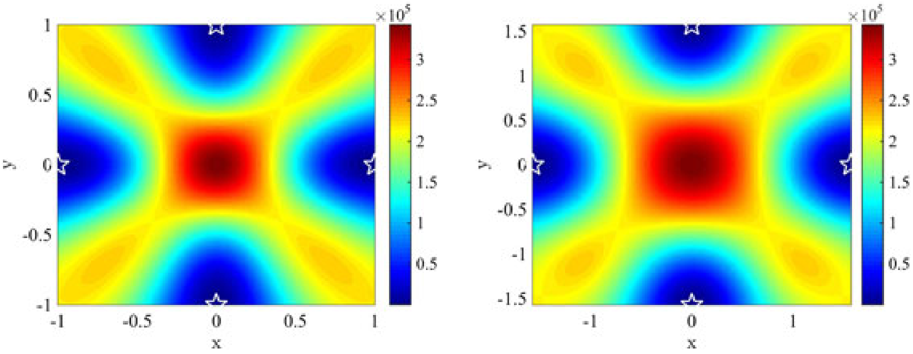

(c) Stereographic (d) Tangent

Figure 6. Plane views of the landscapes of the determinant of the acoustic tensor at bifurcation for simple shear on the small deformation isotropic damage model. The white stars indicate global minima. The normals to the planes of bifurcation are $n_1 = (1, 0, 0)$ and $n_2 = (0, 1, 0)$.

Table II. Isotropic small deformation model: success rate and computation time of the Newton iterative scheme with a single random initial point.

	Spherical	Stereographic	Projective	Tangent	Cartesian
Success rate (%)	12.8	22.7	59.9	20.6	100
Average iteration count	4.39	4.70	8.86	5.12	5.35
Average run time (μs)	211	242	495	264	207

A total of 1000 random trials are performed for each parametrization. Note that the average run time is for successful bifurcation detections only, which is 100% for the Cartesian parametrization.

point within the corresponding parametric space is provided as initial guess for the Newton iterative scheme when $\epsilon_{12} = 0.0559$, that is, at the onset of bifurcation. If Algorithm 1 is able to correctly detect the onset of bifurcation and its associated directions, the parametrization is said to succeed for this one set of randomly generated parameters. This process is repeated 1000 times for each parametrization.

Table II shows the rate of successful bifurcation detection for all five parametrizations. The average number of iterations and the computation time of those successful detections are also recorded and shown in the table. It can be seen that the proposed Cartesian parametrization is much more robust than the commonly used spherical parametrization, compared with 100% vs. 12.8% success rate. Furthermore, the Cartesian parametrization also outperforms the remaining three parametrizations. In terms of computation time, the Cartesian parametrization is efficient with respect to the other tested parametrizations because of its average run time of 207 μs.

The better performance of the proposed Cartesian parametrization in terms of computational efficiency and robustness can be attributed to its relatively simple determinant function landscape.

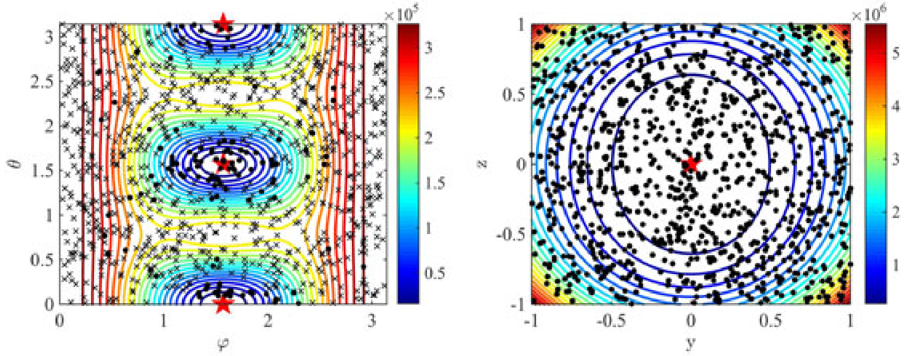

(a) Spherical **(b)** Cartesian

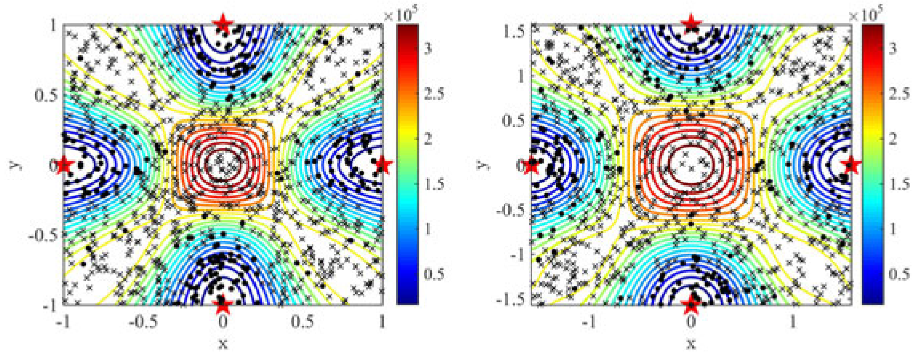

(c) Stereographic **(d)** Tangent

Figure 7. Isotropic small deformation model: results of the Newton iterative scheme with a single random initial guess plotted on contours of the determinant function at bifurcation. A solid circle (●) indicates that the initial point leads to a successful detection of bifurcation and its directions. A cross (×) indicates failure. A total of 1000 random trials are performed for each parametrization.

Figure 7 shows contours of the determinant functions corresponding to Table II. One thousand random initial points are also plotted. If the initial guess leads to a successful detection of bifurcation and its directions, the point is marked as a solid circle (●). Otherwise, it is marked as a cross (×). This figure provides a very direct visualization of the robustness results.

This first example illustrates the performance of different parametrizations on a very simple small deformation material model with tangents possessing both major and minor symmetries. For such material models, an alternative single-stage approach as in [25] could also be applied, which is based on the solution of a coupled eigenvalue problem in terms of the acoustic tensor. A preliminary analysis shows that this approach is able to correctly detect bifurcation and is more computationally efficient than the two-stage approach advanced herein for this type of material models. Our focus, however, is in the full finite deformation case, and therefore, more complex material tangents that do not posses minor symmetries will be investigated next.

5.2. Finite deformation anisotropic hyperelastic damage model

The second material model tested is a finite deformation anisotropic hyperelastic damage model. Our aim is to study the effect of adding complexity to the material model, and hence the tangent moduli, on the performance of the different parametrizations. As in the previous example, we first present the key features of the material model.

5.2.1. Model formulation. The free energy function of the finite deformation anisotropic hyperelastic damage model consists of an isotropic term and direction-dependent terms. The motivation for this type of energy formulation is to capture the behavior of materials with an isotropic matrix and embedded microfibers with preferred directions, such as the model proposed by [38] to describe the behavior of cladding for nuclear reactors subjected to damage by hydride compounds. We assume that the damage affects both the matrix and the microfibers. The free energy function is assumed to have the form

$$A\left(C, M, \xi^{\mathrm{m}}, \xi_i^{\mathrm{f}}\right) := \left(1-\xi^{\mathrm{m}}\right) f^{\mathrm{m}} \Psi^{\mathrm{m}}(C) + \sum_{i=1}^{N} \left(1-\xi_i^{\mathrm{f}}\right) f_i^{\mathrm{f}} \Psi_i^{\mathrm{f}}(C, M) \tag{31}$$

where C is the right Cauchy–Green tensor, M is a unit vector characterizing the preferred fiber direction, f^{m} and f_i^{f} are the volume fraction of the matrix and ith fiber, N is the number of fiber terms, and ξ^{m} and ξ_i^{f} are the damage factors corresponding to the matrix and the ith fibers, respectively. In the following examples, we assume that there are two preferred fiber directions.

We adopt a compressible neo-Hookean type energy function for the effective (undamaged) matrix component

$$\Psi^{\mathrm{m}}(C) = \frac{1}{8}\lambda(\log I_3)^2 - \frac{1}{2}\mu \log I_3 + \frac{1}{2}\mu(I_1 - 3) \tag{32}$$

where λ and μ play the role of the Lamé constants of linear elasticity. For the microfibers, we adopt the particular form of strain-energy function proposed by Holzapfel and Ogden [39]

$$\Psi_i^{\mathrm{f}}(C, M) = \frac{k_i}{q_i} \left\{\exp\left[q_i (I_4 - 1)^2\right]\right\} \tag{33}$$

where k_i and q_i are elastic constants for the ith fiber. The strain invariants I_1, I_3, and I_4 are defined as follows:

$$I_1 = \mathrm{tr} C, \quad I_3 = \det C, \quad I_4 = M \cdot C \cdot M. \tag{34}$$

For the damage parameters, the same evolution law as in (28) is used, except that for each phase of the material, there is a different set of parameters as discussed in [38].

Given the energy function (31), the fourth-order tangent moduli tensor can be derived as follows:

$$\mathbb{C} := (1-\xi^{\mathrm{m}})\mathbb{C}^{\mathrm{m}} - \beta^{\mathrm{m}}\xi^{\mathrm{m}\prime}(S^{\mathrm{m}} \otimes S^{\mathrm{m}}) + \sum_{i=1}^{N} \left[\left(1-\xi_i^{\mathrm{f}}\right)\mathbb{C}_i^{\mathrm{f}} - \beta_i^{\mathrm{f}}\xi_i^{\mathrm{f}\prime}\left(S_i^{\mathrm{f}} \otimes S_i^{\mathrm{f}}\right)\right] \tag{35}$$

where $\beta^{\mathrm{m}} = 1$ if the damage of the matrix evolves within the time increment or $\beta^{\mathrm{m}} = 0$ otherwise, $\beta_i^{\mathrm{f}} = 1$ if the damage of the ith fiber evolves within the time increment or $\beta_i^{\mathrm{f}} = 0$ otherwise, $\xi^{\mathrm{m}\prime}$ and $\xi_i^{\mathrm{f}\prime}$ are the derivatives of the damage parameters defined in (28) with respect to the maximum thermodynamic force defined in (29), and S^{m} and S_i^{f} are the effective (undamaged) second Piola–Kirchhoff stresses for the matrix and the ith fibers given by the following:

$$S^{\mathrm{m}} := 2 f^{\mathrm{m}} \frac{\partial \Psi^{\mathrm{m}}}{\partial C} \tag{36}$$

and

$$S_i^{\mathrm{f}} := 2 f_i^{\mathrm{f}} \frac{\partial \Psi_i^{\mathrm{f}}}{\partial C} \tag{37}$$

where f^{m} and f_i^{f} are the volume fraction of the matrix and ith fiber, respectively.

The effective tangent moduli tensors can be calculated as follows:

$$\mathbb{C}^{\mathrm{m}} := 2 \frac{\partial S^{\mathrm{m}}}{\partial C} \tag{38}$$

and

$$\mathbb{C}_i^{\mathrm{f}} := 2\frac{\partial S^{\mathrm{m}}}{\partial C}. \tag{39}$$

It should be noted that the fourth-order tangent $\mathbb{C}$ from (35) is computed as the second derivative of the strain energy with respect to the right Cauchy–Green deformation tensor C. The strong ellipticity condition (1) requires the tangent $\mathbb{A}$ that is obtained as the second derivative of the strain energy with respect to the deformation gradient F. One tangent can be converted to the other using the following relation (in indicial notation)

$$\mathbb{A}_{ijkl} = S_{lj}\delta_{ik} + F_{ip}\mathbb{C}_{pjlq}F_{kq} \tag{40}$$

where S_{lj} are the components of the second Piola–Kirchhoff stress (including damage contribution) of the corresponding phase (e.g., matrix or fiber component), δ_{ik} is the Kronecker delta, and F_{ij} are the components of the deformation gradient.

5.2.2. Uniaxial tension test. The finite deformation anisotropic model is tested under monotonically increasing uniaxial tension loading illustrated in Figure 8.

The material properties for both the matrix and microfibers are listed in Table III.

The axial stress versus stretch behavior of the uniaxial tension test is shown in Figure 9a, where the X denotes the onset of material bifurcation. We use the two-step procedure together with the adaptive time increment discussed in Section 4 for the detection of bifurcation. Figure 9b shows the degradation of the determinant function for all five parametrizations until material bifurcation is detected. In this loading test, all five parametrizations detect bifurcation at the same time, that is, when the axial component of the deformation gradient $F_{11} = 1.1798$.

As in the previous example, the computation time of the different parametrizations within the loading increment leading to bifurcation is recorded and shown in Table IV. Again, the density of the initial sampling is represented by the sampling interval and the number of sampling points.

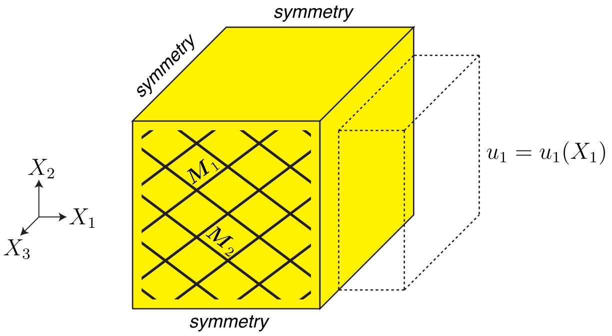

Figure 8. Schematic illustrating the uniaxial tension of a reinforced-fiber composite under finite deformations. Fibers are oriented along $\vec{M}_1$ and $\vec{M}_2$.

Table III. Material properties for anisotropic damage model.

Matrix		Fibers	
Lamé constant	$\lambda = 80$	Elasticity constants	$k_1 = k_2 = 100$
Lamé constant	$\mu = 80$	Elasticity constants	$q_1 = q_2 = 1.0$
Damage variable	$\xi_{\infty}^{\mathrm{m}} = 1.0$	Damage variable	$\xi_{\infty;1}^{\mathrm{f}} = \xi_{\infty;2}^{\mathrm{f}} = 1.0$
Damage variable	$\tau^{\mathrm{m}} = 4.0$	Damage variable	$\tau_1^{\mathrm{f}} = \tau_2^{\mathrm{f}} = 4.0$
Volume fraction	$f^{\mathrm{m}} = 0.2$	Volume fraction	$f_1^{\mathrm{f}} = f_2^{\mathrm{f}} = 0.4$
		Direction vector	$M_1 = (0.8, 0.6, 0.0)$
			$M_2 = (0.8, 0.6, 0.0)$

DOI: 10.1002/nme

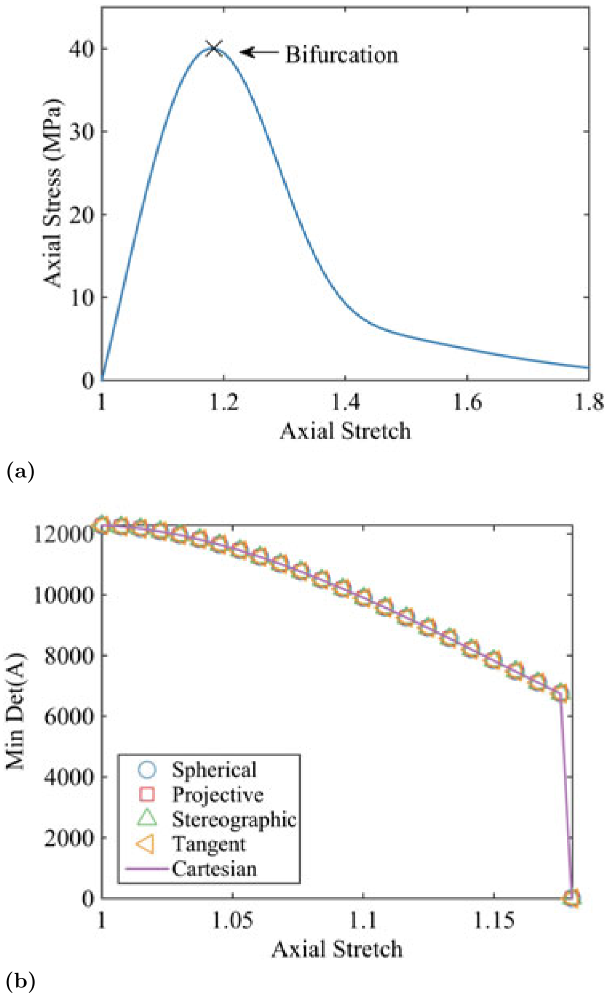

Figure 9. Uniaxial tension test on finite deformation anisotropic damage model: (a)stress versus axial stretch, with the X indicating bifurcation, and (b) degradation of det A for different parametrizations.

Table IV. Computation time for different parametrizations in the uniaxial tension test within the loading increment leading to bifurcation.

Sampling		Total time [µs] Sampling [µs] Newton [µs]				
Interval	Points	Spherical	Stereographic	Projective	Tangent	Cartesian
0.05	41	396 275 121	272 116 156	5832 5648 184	329 183 146	407 330 77
0.10	21	244 83 161	201 31 170	968 783 185	207 51 156	201 99 102
0.20	11	196 30 166	187 9 178	302 111 191	169 17 152	120 25 95
0.30	7	199 12 187	206 4 202	249 28 221	193 6 187	107 11 96
0.40	5	207 7 200	205 2 203	266 11 255	180 3 177	104 6 98

DOI: 10.1002/nme

Table IV. Continued.

Sampling		Total time [μs]				
		Sampling [μs] Newton [μs]				
Interval	Points	Spherical	Stereographic	Projective	Tangent	Cartesian
0.50	5	179 10 169	—	233 11 222	—	120 5 115
0.60	3	181 5 176	172 1 171	228 3 225	190 2 188	193 2 191
0.70	3	211 5 206	170 1 169	190 2 188	143 2 141	117 2 115
0.80	3	—	207 1 206	185 2 183	179 2 177	98 2 96
0.90	3	—	203 1 202	221 3 218	185 2 183	100 2 98
1.00	3	—	—	236 3 233	—	117 2 115
1.50	1	—	—	—	—	—

The dash '–'indicates that the parametrization fails to detect bifurcation in this loading increment. For each interval, the time on the first line is the total run time, and the two smaller numbers below it correspond to the time for initial sampling and the time for the iterative Newton scheme, respectively.

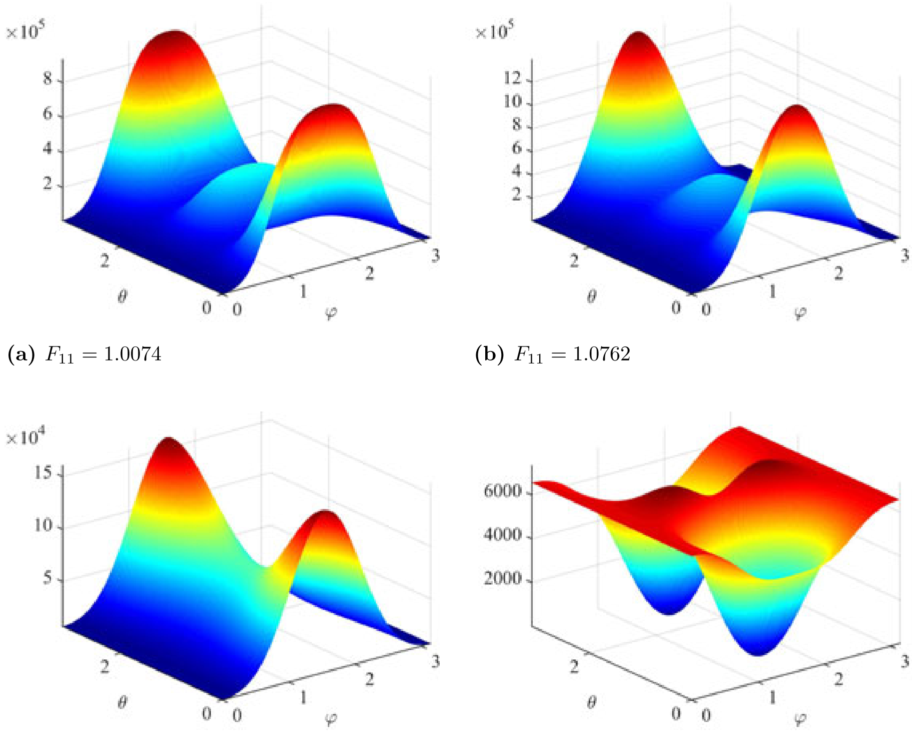

(a) $F_{11} = 1.0074$ (b) $F_{11} = 1.0762$

(c) $F_{11} = 1.1583$ (d) $F_{11} = 1.1798$ (bifurcation)

Figure 10. Spherical parametrization: landscapes of det A for the uniaxial tension test of the finite deformation anisotropic model at different axial stretch levels.

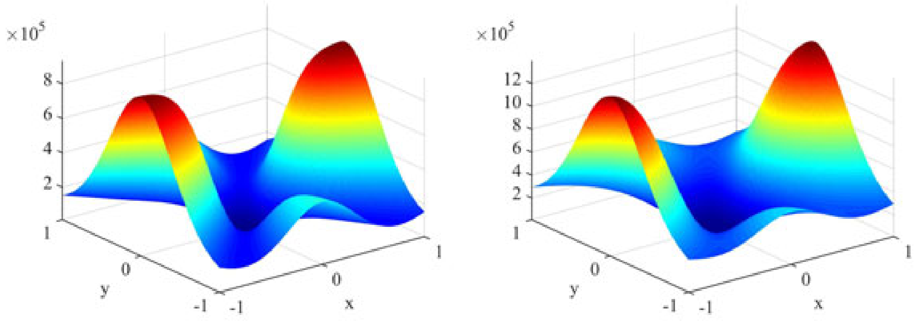

(a) $F_{11} = 1.0074$ (b) $F_{11} = 1.0762$

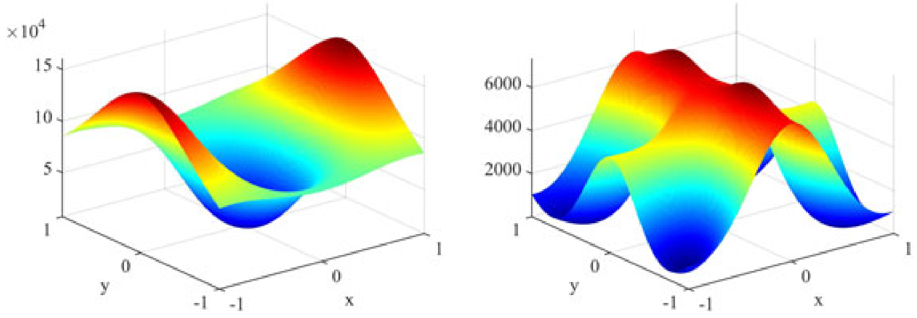

(c) $F_{11} = 1.1583$ (d) $F_{11} = 1.1798$ (bifurcation)

Figure 11. Stereographic parametrization: landscapes of det A for the uniaxial tension test of the finite deformation anisotropic model at different axial stretch levels.

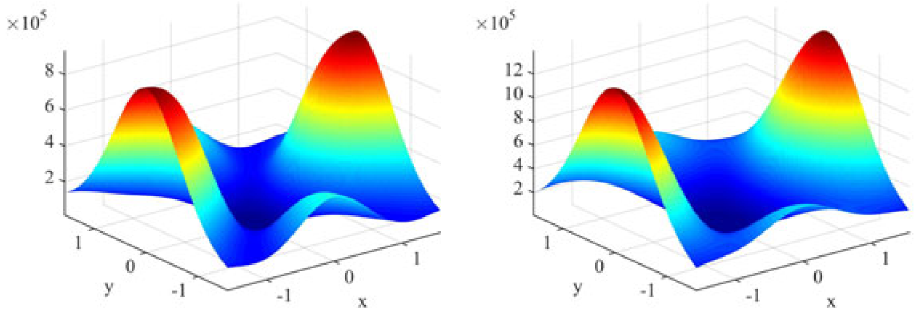

(a) $F_{11} = 1.0074$ (b) $F_{11} = 1.0762$

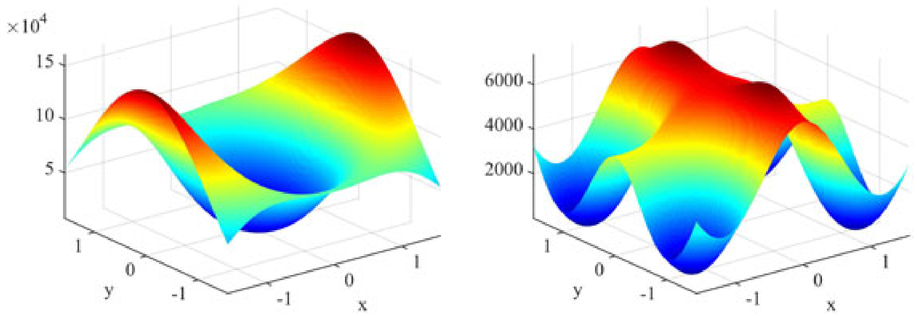

(c) $F_{11} = 1.1583$ (d) $F_{11} = 1.1798$ (bifurcation)

Figure 12. Tangent parametrization: landscapes of det A for the uniaxial tension test of the finite deformation anisotropic model at different axial stretch levels.

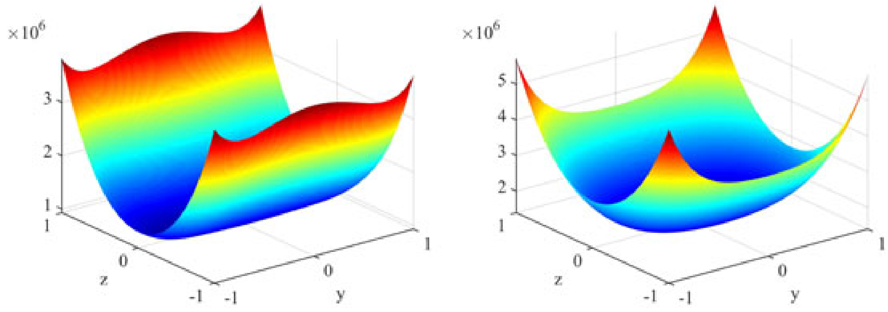

(a) $F_{11} = 1.0074$ **(b)** $F_{11} = 1.0762$

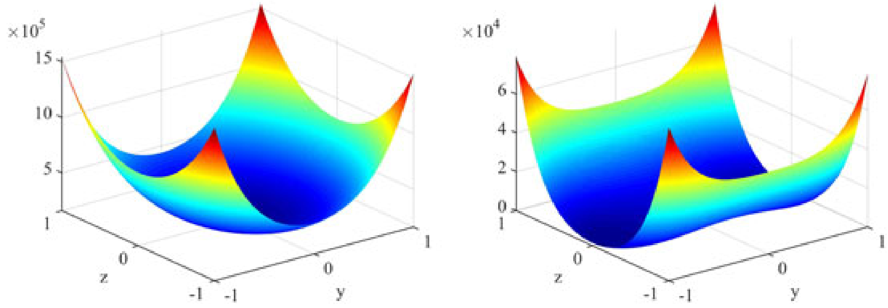

(c) $F_{11} = 1.1583$ **(d)** $F_{11} = 1.1798$ (bifurcation)

Figure 13. Cartesian parametrization: landscapes of det A for the uniaxial tension test of the finite deformation anisotropic model at different axial stretch levels.

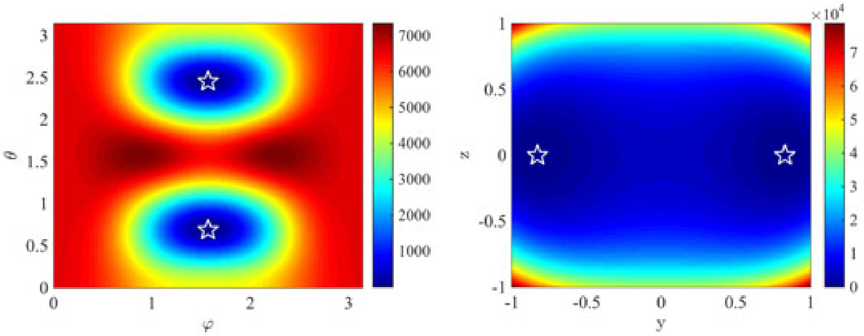

(a) Spherical **(b)** Cartesian

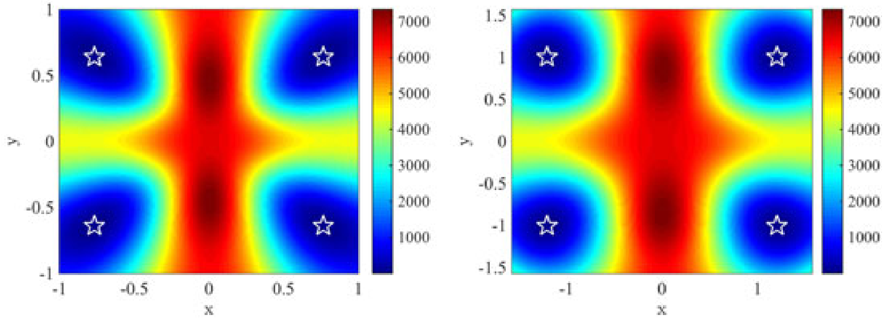

(c) Stereographic **(d)** Tangent

Figure 14. Plane views of the landscapes of the determinant of the acoustic tensor at bifurcation for the uniaxial tension on the finite deformation anisotropic model. The white stars indicate global minima at $n_1 \approx (0.768, -0.641, 0.000)$ and $n_2 \approx (0.768, 0.641, 0.000)$.

In addition to the total computation time, the time for the initial sampling stage and the iterative Newton scheme are also reported. In general, as the number of sampling points decreases, so does the total computation time. Fewer sampling points, however, may lead to a poor initial guess for the Newton iterative scheme, which may result in a greater overall computation time to arrive at a converged solution. Also, it is observed that, except for the very dense sampling case (interval=0.05), most of the computation time is spent on the second stage, that is, the iterative Newton scheme. Because of the added complexity of the material model, different parametrizations are more sensitive to the density of the initial sampling grids. The spherical parametrization fails to correctly detect the bifurcation when the sampling interval is greater than 0.6. The stereographic, projective, and tangent parametrizations, although more robust in this case, are computationally more expensive. The Cartesian parametrization is the most efficient in terms of the total computation time and the time spent on the iterative Newton scheme. At the same time, this parametrization is relatively insensitive to the sampling intervals.

To gain insight into the influence of the parametrizations on the determinant function det A as loading proceeds, we plot in Figures 10–13 the landscapes at four different axial stretch levels for different parametrizations. Moreover, the corresponding plane views of the determinant landscapes at the bifurcation are also shown in Figure 14, where the white stars indicate global minima.

Table V. Anisotropic finite deformation model: success rate and computation time of the Newton iterative scheme with a single random initial guess.

	Spherical	Stereographic	Projective	Tangent	Cartesian
Success rate (%)	13.4	32.3	71.5	32.3	74.4
Average iteration count	4.37	4.91	8.04	4.57	6.93
Average run time (μs)	270	274	483	245	267

A total of 1000 random trials are performed for each parametrization.

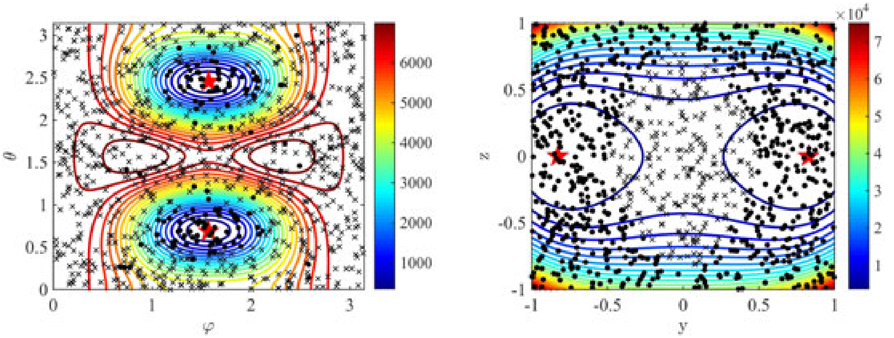

(a) Spherical

(b) Cartesian

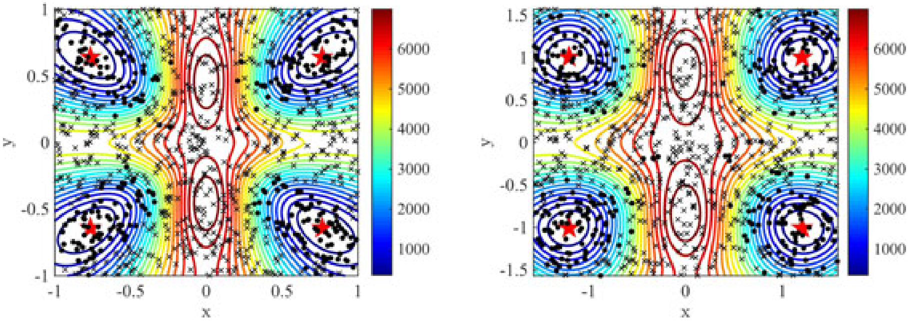

(c) Stereographic

(d) Tangent

Figure 15. Anisotropic finite deformation model: results of the Newton iterative scheme with a single random initial guess plotted on contours of the determinant function at bifurcation. A solid circle (●) indicates that the initial point leads to a successful detection of bifurcation and its directions. A cross (×) indicates failure. A total of 1000 random trials are performed for each parametrization.

As can be seen from Figure 13, the Cartesian parametrization again results in a simple bowl-shaped landscape of the determinant function consistently throughout the loading process, which is in contrast to the more complex landscapes of the spherical (Figure 10), stereographic (Figure 11), and tangent (Figure 12) parametrizations. Note that for the Cartesian parametrization, the two global minima are separated by a very small ridge. Although our method is able to detect multiple global minima, the implementation stops when finding the first of the multiple minima, which is sufficient for the purpose of identification of the bifurcation condition.

As in the case of the small deformation model example in Section 5.1, the robustness of the different parametrizations on the detection of material bifurcation is analyzed by randomly generating a single initial point for the Newton iterative scheme and eliminating the initial sampling. A total of 1000 random initial guesses are generated for each parametrization. The success rate and computation time are recorded and summarized in Table V. The results are consistent with the small deformation model example, that is, the Cartesian parametrization is the most robust and computationally efficient of all the ones tested.

A visualization of the robustness of each parametrization with 1000 random initial guesses is shown in Figure 15. If the initial guess leads to a successful detection of bifurcation and its directions, the point is marked as a solid circle (●). Otherwise, it is marked as a cross (×).

As in the case of the small deformation model example in Section 5.1, the Cartesian parametrization performs better in terms of trade-off between computational efficiency and robustness. In a nonlinear large-scale finite element simulation, this optimal trade-off between computational efficiency and robustness becomes critical. We note that for this finite deformation example, the single-stage approach of [25] cannot correctly detect the bifurcation time nor the bifurcation direction. The Cartesian parametrization thus provides a valuable tool in numerical bifurcation analysis.

6. CONCLUSION

In this work, we examine the numerical performance of five different parametrizations for the detection of the loss of the ellipticity condition for the analysis of material instabilities. An algorithm based on an initial sampling on a parametric grid followed by an iterative Newton scheme is introduced as a robust and efficient method for the detection of the bifurcation condition. In addition, we introduce a new parametrization that we term Cartesian for the representation of the normal vector that defines the acoustic tensor in terms of the tangent moduli tensor. We demonstrate with numerical examples that the Cartesian parametrization offers the best performance in terms of computational efficiency and robustenss as compared with other four parametrizations. In summary, we find that

1. The classical bifurcation condition by means of the acoustic tensor can be used for a very general class of materials that include viscoelasticity, viscoplastiticy, and rate dependence by recourse to incremental varriational constitutive updates.
2. Idealized isotropic and anisotropic damage models subjected to simplified loadings provided sufficient complexity to evaluate the proposed parametrizations for minimization.
3. The parametrization of the normal vector significantly affects the complexity of the objective function to be minimized, which in turn influences the computational efficiency and robustness of the algorithm used for the detection of bifurcation.
4. The commonly used spherical parametrization is efficient provided that the initial sampling interval is fine enough and the initial guess is a good approximation to the minimum. This parametrization, however, suffers from singularities for the representation of points at its poles.
5. The stereographic and tangent parametrizations are the least robust, that is, they are more likely to have convergence issues. The projective parametrization is much more expensive.
6. The Cartesian parametrization is the most robust for the material models and loading conditions tested. It does not have any singularities, and it is also computationally efficient. The Cartesian parametrization represents an optimal trade-off between computational efficiency and robustness and provides a valuable tool for efficient and robust numerical analysis of material instability in a large-scale finite element analysis.

Future work will develop the computational infrastructure necessary to extend our current work on inelastic constitutive models undergoing large deformations to the complex loadings that accompany the fracture and failure of engineering structures.

ACKNOWLEDGEMENTS

Support for this work was received through the US Department of Energy's (DOE) Advanced Simulation and Computing (ASC) Program at Sandia National Laboratories. Sandia National Laboratories is a multi-program laboratory managed and operated by Sandia Corporation, a wholly owned subsidiary of Lockheed Martin Corporation, for the US Department of Energy's National Nuclear Security Administration under contract DE-AC04-94AL85000.

APPENDIX A: VARIATIONAL CONSTITUTIVE UPDATES

The mechanical response of the solids considered here is characterized by a dissipation potential of the form

$$D(F, \dot{F}, Z, \dot{Z}) := \dot{A}(F, Z) + \phi(F, \dot{F}, Z) + \psi^*(Z, \dot{Z}), \tag{A.1}$$

in which $A(F, Z)$ is the Helmholtz free-energy density, $\phi(F, \dot{F}, Z)$ is a viscous potential, $\psi^*(Z, \dot{Z})$ is a dual-kinetic potential or dissipation function, F is the deformation gradient, and Z is a collection of suitable internal variables that describe the state of the material at a given point. The first Piola–Kirchhoff stress and the conjugate thermodynamic forces to Z are given by the following:

$$P := \frac{\partial D}{\partial \dot{F}}(F, \dot{F}, Z, \dot{Z}) = \frac{\partial A}{\partial F}(F, Z) + \frac{\partial \phi}{\partial \dot{F}}(F, \dot{F}, Z), \quad Y := -\frac{\partial A}{\partial Z}(F, Z), \tag{A.2}$$

respectively. In order to ensure a variational structure, we have postulated the existence of a dual-kinetic potential or dissipation function $\psi^*(Z, \dot{Z})$ such that

$$Y = \frac{\partial \psi^*}{\partial \dot{Z}}(Z, \dot{Z}). \tag{A.3}$$

Next, we minimize the dissipation potential (A.1) with respect to the internal variable rates as follows:

$$\begin{aligned} \inf_{\dot{Z}}[D(F, \dot{F}, Z, \dot{Z})] &= \inf_{\dot{Z}}\left[\dot{A}(F, Z) + \psi^*(Z, \dot{Z})\right] + \phi(F, \dot{F}, Z), \\ &= \inf_{\dot{Z}}\left[\frac{\partial A}{\partial F}(F, Z) : \dot{F} + \frac{\partial A}{\partial Z}(F, Z) \cdot \dot{Z} + \psi^*(Z, \dot{Z})\right] + \phi(F, \dot{F}, Z). \end{aligned} \tag{A.4}$$

This is equivalent to stating that the internal variables should not produce any net work, that is,

$$\left[\frac{\partial A}{\partial Z}(F, Z) + \frac{\partial \psi^*}{\partial \dot{Z}}(Z, \dot{Z})\right] \cdot \dot{Z} = 0 \quad \forall \dot{Z}, \tag{A.5}$$

which in turn leads to Biot's equation for standard dissipative systems

$$\frac{\partial A}{\partial Z}(F, Z) + \frac{\partial \psi^*}{\partial \dot{Z}}(Z, \dot{Z}) = 0. \tag{A.6}$$

Approximate solutions to (A.6) may be found by recourse to the incremental energy density function for a time increment $t \in [t_n, t_{n+1}]$

$$w(F_{n+1}, Z_{n+1}) := \int_{t_n}^{t_{n+1}} \left[\dot{A}(F, Z) + \phi(F, \dot{F}, Z) + \psi^*(Z, \dot{Z})\right] \mathrm{d}t, \tag{A.7}$$

in which the integral is evaluated using a midpoint-like rule as follows:

$$\begin{aligned} w(F_{n+1}, Z_{n+1}) \approx\, & A(F_{n+1}, Z_{n+1}) - A(F_n, Z_n) + \\ & \triangle t\left[\phi\left(F_{n+\alpha}, \frac{\triangle F}{\triangle t}, Z_{n+\alpha}\right) + \psi^*\left(Z_{n+\alpha}, \frac{\triangle Z}{\triangle t}\right)\right] \end{aligned} \tag{A.8}$$

with

$$\triangle t := t_{n+1} - t_n, \quad \triangle F := F_{n+1} F_n^{-1}, \quad \triangle Z := Z_{n+1} - Z_n, \tag{A.9}$$

and

$$\begin{aligned} F_{n+\alpha} &:= \exp[(1-\alpha)\log\, F_n + \alpha \log\, F_{n+1}], \\ Z_{n+\alpha} &:= (1-\alpha)\, Z_n + \alpha\, Z_{n+1}, \end{aligned} \tag{A.10}$$

where α is an algorithmic parameter. The implicit assumption in this interpolation is that the deformation gradient F belongs to a Lie group and thus requires the exponential and logarithmic maps for its proper interpolation, whereas the internal variables Z belong to a space that admits direct linear interpolation [40]. In order to obtain an explicit scheme, we choose $\alpha = 0$. Next, we define the incremental stress potential as follows:

$$\begin{aligned} W(F_{n+1}) := &\inf_{Z_{n+1}} [w(\,F_{n+1},\; Z_{n+1})] \\ = &\inf_{Z_{n+1}} \left[A(\,F_{n+1},\; Z_{n+1}) - A(\,F_n,\; Z_n) + \triangle t \psi^* \left(Z_n, \frac{\triangle\, Z}{\triangle t} \right) \right] + \\ &\triangle t \phi \left(F_n, \frac{\triangle\, F}{\triangle t},\; Z_n \right). \end{aligned} \tag{A.11}$$

This minimization provides an optimal path for the internal variables Z in the time increment $t \in [t_n, t_{n+1}]$. Furthermore, the Euler–Lagrange equation corresponding to (A.11) is

$$\frac{\partial A}{\partial\, Z_{n+1}}(\,F_{n+1},\; Z_{n+1}) + \triangle t \frac{\partial \psi^*}{\partial\, Z_{n+1}} \left(Z_n, \frac{\triangle\, Z}{\triangle t} \right) = 0, \tag{A.12}$$

which is a discrete version of Biot's equation (A.6) [41]. The incremental first Piola–Kirchhoff stress and tangent moduli can be computed in turn as follows:

$$P_{n+1} := \frac{\partial W}{\partial\, F}(\,F_{n+1}), \quad \mathbb{A}_{n+1} := \frac{\partial^2 W}{\partial\, F^2}(\,F_{n+1}), \tag{A.13}$$

respectively.

REFERENCES

1. Simo JC, Oliver J, Armero F. An analysis of strong discontinuities induced by strain-softening in rate-independent inelastic solids. *Computational Mechanics* 1993; **12**(5):277–296.
2. Oliver J. Modelling strong discontinuities in solid mechanics via strain softening constitutive equations. part 1: fundamentals. *International Journal for Numerical Methods in Engineering* 1996; **39**(21):3575–3600.
3. Oliver J. Modelling strong discontinuities in solid mechanics via strain softening constitutive equations. part 2: Numerical simulation. *International journal for numerical methods in engineering* 1996; **39**(21):3601–3623.
4. Armero F, Garikipati K. An analysis of strong discontinuities in multiplicative finite strain plasticity and their relation with the numerical simulation of strain localization in solids. *International Journal of Solids and Structures* 1996; **33**(20-22):2863–2885.
5. Moës N, Belytschko T. Extended finite element method for cohesive crack growth. *Engineering Fracture Mechanics* 2002; **69**(7):813–833.
6. Foster CD, Borja RI, Regueiro RA. Embedded strong discontinuity finite elements for fractured geomaterials with variable friction. *International Journal for Numerical Methods in Engineering* 2007; **72**(5):549–581.
7. Chen Q, Andrade JE, Samaniego E. AES for multiscale localization modeling in granular media. *Computer Methods in Applied Mechanics and Engineering* 2011; **200**(33):2473–2482.
8. Antman S. *Nonlinear Problems in Elasticity*, Second. Springer: New York, 2005.
9. Hill R. Acceleration waves in solids. *Journal of the Mechanics and Physics of Solids* 1962; **10**(1):1–16.
10. Ortiz M, Stainier L. The variational formulation of viscoplastic constitutive updates. *Computer Methods in Applied Mechanics and Engineering* 1999; **171**(3-4):419–444.
11. Lambrecht M, Miehe C, Dettmar J. Energy relaxation of non-convex incremental stress potentials in a strain-softening elastic-plastic bar. *International Journal of Solids and Structures* 2003; **40**(6):1369–1391.
12. Miehe C, Lambrecht M, Gürses E. Analysis of material instabilities in inelastic solids by incremental energy minimization and relaxation methods: evolving deformation microstructures in finite plasticity. *Journal of the Mechanics and Physics of Solids* 2004; **52**(12):2725–2769.
13. Weinberg K, Mota A, Ortiz M. A variational constitutive model for porous metal plasticity. *Computational Mechanics* 2006; **37**:142–152.
14. Fancello E, Ponthot JP, Stainier L. A variational formulation of constitutive models and updates in non-linear finite viscoelasticity. *International Journal for Numerical Methods in Engineering* 2006; **65**(11):1831–1864.
15. Mosler J, Bruhns OT. On the implementation of rate-independent standard dissipative solids at finite strain – variational constitutive updates. *Computer Methods in Applied Mechanics and Engineering* 2010; **199**(9-12): 417–429.

16. Bleier N, Mosler J. Efficient variational constitutive updates by means of a novel parameterization of the flow rule. *International Journal for Numerical Methods in Engineering* 2012; **89**(9):1120–1143.
17. Hadamard J. *Leçons sur la Propagation des Ondes et les Équations de L'hydrodynamique*. Hermann: Paris, 1903.
18. Thomas TY. *Plastic Flow and Fracture in Solids*. Academic Press: London, 1961.
19. Rudnicki JW, Rice JR. Conditions for the localization of deformation in pressure-sensitive dilatant materials. *Journal of the Mechanics and Physics of Solids* 1975; **23**(6):371–394.
20. Rice JR. The Localization of Plastic Deformation. In *Proceedings of the 14th International Congress on Theoretical and Applied Mechanics*, Vol. 1, Koiter, WT (ed.). North-Holland: Amsterdam, 1976; 207–220.
21. Schreyer HL, Neilsen MK. Analytical and numerical tests for loss of material stability. *International Journal for Numerical Methods in Engineering* 1996; **39**(10):1721–1736.
22. Becker R. Ring fragmentation predictions using the Gurson model with material stability conditions as failure criteria. *International Journal of Solids and Structures* 2002; **39**(13-14):3555–3580.
23. Oliver J, Huespe AE. Theoretical and computational issues in modelling material failure in strong discontinuity scenarios. *Computer Methods in Applied Mechanics and Engineering* 2004; **193**(27):2987–3014.
24. Xue L, Belytschko T. Fast methods for determining instabilities of elastic–plastic damage models through closed-form expressions. *International Journal for Numerical Methods in Engineering* 2010; **84**(12):1490–1518.
25. Oliver J, Huespe AE, Cante JC, Diaz G. On the numerical resolution of the discontinuous material bifurcation problem. *International Journal for Numerical Methods in Engineering* 2010; **83**(6):786–804.
26. Ortiz M. An analytical study of the localized failure modes of concrete. *Mechanics of Materials* 1987; **6**(2):159–174.
27. Ortiz M, Leroy Y, Needleman A. A finite-element method for localized failure analysis. *Computer Methods in Applied Mechanics and Engineering* 1987; **61**(2):189–214.
28. Khen R, Désoyer T, Dragon A. Objective localization criterion and behavior for finite deformation plasticity–a lagrangian formulation. *Archive of Applied Mechanics* 1998; **68**(2):85–102.
29. Boussaa D, Aravas N. A numeric-symbolic approach to the problem of localization of plastic flow. *Computational Mechanics* 2001; **27**(4):324–331.
30. Mosler J. Numerical analyses of discontinuous material bifurcation: strong and weak discontinuities. *Computer Methods in Applied Mechanics and Engineering* 2005; **194**(9):979–1000.
31. Truesdell C, Noll W. *The Non-linear Field Theories of Mechanics*. Springer-Verlag: Berlin Heidelberg, 2004.
32. Andrade JE, Borja RI. Capturing strain localization in dense sands with random density. *International Journal for Numerical Methods in Engineering* 2006; **67**(11):1531–1564.
33. Springmann M, Kühhorn A, Kuna M, Scherzer M. Influence of strain localization on parameter identification. *Journal of Engineering Materials and Technology* 2009; **131**(1):011003.
34. Regueiro RA, Foster CD. Bifurcation analysis for a rate-sensitive, non-associative, three-invariant, isotropic/kinematic hardening cap plasticity model for geomaterials: Part i. small strain. *International Journal for Numerical and Analytical Methods in Geomechanics* 2011; **35**(2):201–225.
35. Simo JC, Fox DD. On a stress resultant geometrically exact shell-model part I. Formulation and Optimal Parametrization. *Computer Methods in Applied Mechanics and Engineering* 1989; **72**(3):267–304.
36. Gallier J. *Geometric Methods and Applications: For Computer Science and Engineering*. Springer: New York, 2011.
37. Holzapfel GA. *Nonlinear Solid Mechanics: A Continuum Approach for Engineering*, Vol. 24. Wiley: Chichester, 2000.
38. Chen Q, Ostien JT, Hansen G. Development of a used fuel cladding damage model incorporating circumferential and radial hydride responses. *Journal of Nuclear Materials* 2014; **447**(1):292–303.
39. Holzapfel GA, Ogden RW. Constitutive modelling of arteries. *Proceedings of the Royal Society A Mathematical, Physical and Engineering Sciences* 2010; **466**:1551–1597.
40. Mota A, Sun W, Ostien JT, Foulk III J W, Long KN. Lie-group interpolation and variational recovery for internal variables. *Computational Mechanics* 2013; **52**(6):1281–1299.
41. Miehe C, Schotte J, Lambrecht M. Homogenization of inelastic solid materials at finite strains based on incremental minimization principles. Application to the texture analysis of polycrystals. *Journal of the Mechanics and Physics of Solids* 2002Oct; **50**(10):2123–2167.

DOI: 10.1002/nme